Tracking the Redox Properties of CeO_2 Powders by Infrared Spectroscopy: Monitoring the Defect States by O_2 Adsorption and the Ce^{3+} Spin–Orbit Transition

Lachlan Caulfield, Eric Sauter, Hicham Idriss,* and Christof Wöll*

ABSTRACT: In recent years, considerable attention has been given to the role of oxygen defect centers of oxides in photocatalysis, electrocatalysis, and related materials performance studies. CeO_2 is one of the text book examples of oxygen defects (and associated Ce^{3+} cations). In this work, we revisit this in order to quantify these defect centers and obtain fundamental data that may help in designing new materials. O_2 adsorption on reduced polycrystalline cerium oxide (CeO_{2-x}) was therefore monitored using diffuse reflectance IR spectroscopy at different temperatures and pressures via the stretch vibration of surface superoxo species (1125 cm^{-1}). Ce^{3+} cations of the ceria particles were monitored from the intensity of the spin–orbit electronic transition ($^2F_{5/2}$ to $^2F_{7/2}$), in the 2050–2200 cm^{-1} range. This latter signal was attenuated upon adsorption of O_2 and nearly disappeared at full coverage. The isosteric heat of adsorption of O_2 to the superoxo species was found to be about 0.7 eV at near-surface saturation. Moreover, the relationship between the appearance of the superoxo species and the disappearance of the spin–orbit transition of Ce^{3+} cations at different temperatures was found to be inverted. While higher O_2 pressures are needed at higher temperatures for surface saturation, lower O_2 pressures are needed at higher temperatures for the disappearance of the Ce^{3+} cations signal. Both trends may be explained as being due to the dissociation of O_2 followed by atomic oxygen diffusion into the bulk of CeO_{2-x}. The IR signal of O_2 adsorption on CeO_{2-x} is therefore not simply due to titration of static surface Ce^{3+} sites but has a component of oxidation reaction in it.

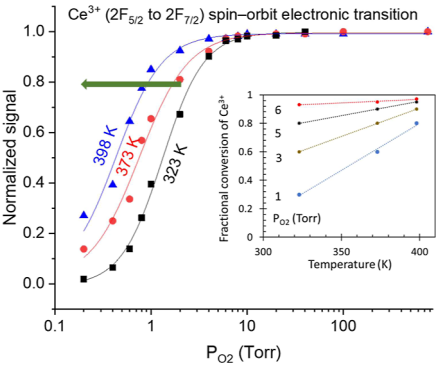

INTRODUCTION

CeO_2 stands out as one of the most stable reducible oxides known, lending itself to a variety of uses, ranging from heterogeneous catalysis to solar-thermal materials and sensors. Its effectiveness in diverse roles—such as a three-way catalyst,[1] a water gas shift reaction catalyst,[2] or a thermochemical water-splitting oxide,[3] is due to a shared characteristic: the ability to abstract and recover oxygen atoms from its surface and lattice.

Much work is devoted at the computational[4] and experimental[5] levels to probe into this property in order to link it to specific reactions or, as in many cases, to provide fundamental information needed to improve our understanding. Experimental research exploring its redox properties has utilized techniques such as photoelectron spectroscopy[6] (specifically X-ray and ultraviolet photoelectron spectroscopies, XPS and UPS), electron spin resonance,[7] and UV–vis absorbance.[8]

In photoelectron spectroscopy, the analysis of Ce 3d core electrons and Ce 4f valence electrons is primarily used for near-surface and surface studies, which have significantly enhanced our understanding of this redox property. Key findings include the observation that a reduced surface exhibits high reactivity toward reactants (such as CO_2 reduction and oxidative dehydrogenation of alcohols to aldehydes[9]). Moreover, cerium oxide provides a stable Lewis acid–base adsorption sites (Ce^{4+}–O^{2-}) for reactants.[10] These two combined properties together with its stability make it one of the most useful oxides to study.

Computationally, it has been recognized early on that the coordination number of Ce cations of CeO_2 (which has a fluorite structure) plays a crucial role in the surface stability (surface energy)[11] where the (111) terminated is more stable than the (110) followed by the (100) (a reconstructed surface, with its exact atomic positions still under study).[12,13]

Experimentally, reduction occurs upon heating at high temperatures under vacuum (typically 1000 °C or close) or in the presence of a reducing agent (such as H_2 or CO) at lower temperatures because of the chemical energy that these molecules provide.[14]

The reduction of CeO_2 (like other reducible oxides) occurs upon removal of oxygen atoms. Because the electron affinity of O^- in the gas phase is positive (+845 kJ/mol or 8.7 eV),[15] the $Ce^{4+}-O^{2-}$ bond dissociation leaves behind electrons and, for each O atom, it removed two electrons, which are left in the lattice. The removed O atoms recombine and desorb as molecular oxygen. The two electrons left are shared by two Ce cations with locations depending on several factors including coordination number and unit lattice dimension (compression and expansion).[16]

There are a few key properties to consider for such a process. Among the most studied are the following. The energy needed to remove oxygen atoms, the energy needed to diffuse them, and the stability of the reduced surface. Typically, the cost of a bulk reduction was computed and values between 4.0 and 3.0 eV are reported depending on the method used [DFT + U_{eff}][17] and hybrid functions (DFT and HF)[18]. Also, the cost of removing a surface oxygen atom or an oxygen atom from the second layer has been studied, and it was observed that (111), which is composed exclusively of oxygen anions, three-fold coordinated to Ce cations of the layer below, does not stabilize oxygen vacancies.[19] The activation energy for oxygen diffusion in CeO_2 has been measured and computed also many decades ago.[20] Energies close to 1 eV have been reported; which is small when compared to the energy cost of removing oxygen atoms from the bulk. In other words, for practical purposes, it is not a limiting factor in the reduction process but can be important in the reoxidation side of the process.

The binding energy of neutral oxygen molecules on oxidized surfaces is under 0.1 eV, necessitating temperatures well below room temperature. However, on reduced oxide (CeO_{2-x} in this case), the situation changes and charge transfer can stabilize adsorbed O_2 as superoxo ($O_2^{-\cdot}$) species, at ca. 1130 cm^{-1} and peroxo ($O_2^{-\cdot\cdot}$), at ca. 850 cm^{-1}, adsorbates. These were studied on both powder and single crystals by infrared and Raman spectroscopy.[21−25] These two species were observed on reduced CeO_2(110) and (100) but not on the reduced CeO_2(111) single crystals.[26] Also, it has been noticed by many researchers that the peroxo species is more pronounced on heavily reduced CeO_2, relative to the superoxo species. The interaction of O_2 with reduced ceria results in the formation of a paramagnetic O_2^- superoxo species or of a diamagnetic O_2^{2-} peroxo species. Each oxygen vacancy (V_O) in reduced CeO_2 is associated with the formation of two $Ce^{3+}-4f^1$ ions. The O_2 molecule interacts with V_O where the molecule is adsorbed with one O atom filling the vacancy and the other pointing out from the surface, in the case of the superoxo (η^1) or when both O atoms bonded to the surface (η^2) in the case of the peroxo. A detailed discussion on these and the associated energetics has been given previously.[27] CeO_{2-x} exhibits an IR-active electronic excitation at ca. 2050−2200 cm^{-1}. This is due to Ce^{3+} ($^2F_{5/2}$ to $^2F_{7/2}$) spin−orbit electronic transition.[28−30] Therefore, one can monitor the appearance of the superoxo and/or peroxo bands and the disappearance of the electronic transition band at the same time.[31]

We are not aware of reported experimental results for the adsorption energy of O_2 on oxidized or reduced CeO_2 powder. This quantity can be computed using the Clausius−Clapeyron equation as has been conducted for other molecules in which the adsorption is pressure-dependent.[32] In this work, we studied O_2 adsorption on CeO_{2-x} powder at different pressures and temperatures in order to extract the adsorption energy at different coverages. In addition, the decay of the electronic transition (of Ce^{3+} actions) was monitored to help understand the fundamentals behind CeO_{2-x} oxidation via the diffusion of O atoms into the interior of the ceria powder particles.

Methodology. Diffuse reflectance infrared Fourier transform spectroscopy (DRIFTS) measurements were performed in a VERTEX80 FTIR (Bruker) equipped with Praying Mantis diffuse reflection optics (Harrick) and a liquid-nitrogen-cooled mercury cadmium telluride detector (LN-MCT). For the DRIFTS measurements, the powder sample was placed in a high-temperature in situ cell (Harrick) covered with ZnS_2 windows. The powder temperature is controlled by a heating cartridge below the cell and by a water circulation system. Polycrystalline ceria powder from Solvay (BET surface area = ca. 100 m^2/g, and particle size = ca. 10 nm) was pressed into small pellets. Figures S1 and S2 present XRD and scanning electron microscopy (SEM) images of CeO_2. TEM images of this CeO_2 were reported by others.[33,34] To ensure that samples do not detach from the holder and prevent samples from dislodging, the pellets are subsequently crushed to create large flakes, which improve the diffuse reflectance. The ceria flakes are then weighed, approximately 100 mg, using a microbalance.

After transfer, the DRIFTS cell is evacuated by using a SH-112 Dry Scroll Pump, achieving a pressure of ca. 10^{-2} Torr. Subsequently, the pressure is reduced to ca. 10^{-5} Torr using a turbomolecular pump. A background IR spectrum (256 scans, 4 cm^{-1} resolution) of the untreated sample is recorded at 25 °C. Thermal reduction is performed by heating the powder samples to 1073 K under vacuum for 60 min before cooling to a desired temperature for exposure to O_2. Reduction is conducted under vacuum in the absence of H_2 in order to minimize the formation of surface hydroxyls as they have shown to affect O_2 adsorption.[35] A second reference spectrum (256 scans, 4 cm^{-1} resolution) is recorded and used as the background for the IR absorbance spectra recorded in the next steps. Before backfilling the chamber with O_2 [>99% O_2 (Linde)] at different pressures up to about 760 Torr, the lines to both pumps are closed. At this point, continuous recording of spectra (256 scans, 4 cm^{-1} resolution, each taking ca. 50 s) started. After saturation of the IR signals was achieved, the cell was again opened to the pumps, restoring a base pressure of ca. 10^{-5} Torr. Subsequently, further IR spectra were recorded to investigate the desorption process of remaining adsorbates.

O_2 adsorption energies were determined from the superoxo coverage (which is assumed to be proportional to the 1125 cm^{-1} absorption band) at different sample temperatures using the Clausius−Clapeyron equation[36] (the isosteric differential heat of adsorption method). Thus, the equilibrium pressure (P) versus temperature (T) at constant coverage (θ) is given as follows: $\frac{dp}{p} = -\frac{\Delta H}{RT^2}dT$ or $d(\ln p)_\theta = -\frac{\Delta H}{R}d\left(\frac{1}{T}\right)_\theta$. In practical terms, the isotherm of the adsorbed O_2 signal obtained from the peak intensity is plotted as a function of the O_2 pressure (P_{O_2}) at different temperatures. Then, the different pressure values needed to obtain a constant coverage are plotted as a function of $1/T$.

RESULTS AND DISCUSSION

Figure 1 shows spectra recorded at different pressures of O_2 at 300 K. Only the superoxo band at 1125 cm^{-1} is seen, and the

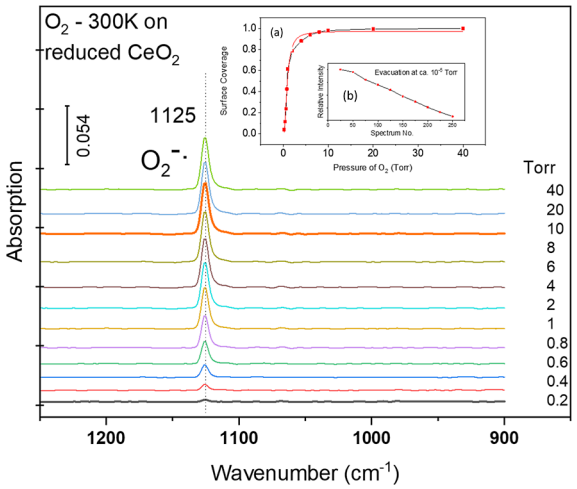

Figure 1. Changes of the superoxo species at 1125 cm^{-1} upon O_2 adsorption on reduced CeO_2 at 300 K at the indicated pressures. Surface saturation is reached at ca. 10 Torr [inset (a)]. The inset (b) shows decrease of the 1125 cm^{-1} peak upon evacuation at 300 K.

peroxo band found at 885 cm^{-1} for CeO_2(110) single-crystal surfaces was not observed here. We explain the absence of this peroxo band to the mild reduction conditions in our case and/or to the absence of (110)-oriented facets on the powder particles studied here. While information is available on the surface orientations of CeO_2 nanoparticles of defined shapes (such as nano-octahedra,[37] nanorods,[38] and nanocubes[39]), much less is known on the structure of their reduced states. A study conducted by environmental TEM on predominantly orientated (111) nanoparticles of CeO_2 has shown considerable flattening of their surface which become mostly (110) terminated upon reduction at 720 °C under 0.5 Torr of H_2 and then cooled to 873 K under H_2.[40] The superoxo band increases with an increasing O_2 pressure on CeO_{2-x} until it saturates at about 10 Torr. The inset (a) in Figure 1 shows the normalized intensity (surface coverage). The coverage dependence of the 1125 cm^{-1} peak is well reproduced by a Langmuir-type function; the fit yields R^2 = 0.99. Upon evacuation of O_2 gas, the signal disappears at 300 K with time [see the inset (b) in Figure 1].

Figure 2 shows the IR band in the 2050−2200 cm^{-1} range related to the Ce^{3+} ($^2F_{5/2}$ to $^2F_{7/2}$) spin−orbit transition signal as a function of O_2 pressure at 300 K. The data shown are obtained upon the subtraction of the actual data from a reference spectrum recorded just before exposure to O_2 and is therefore a measure of [Ce^{3+}] consumption (by removal of an electron to yield Ce^{4+}). Unlike the O_2 superoxo band, the shape of the signal is complex, with multiple peaks attributed to Ce^{3+} in different environments by others.[30] For the quantitative determination of Ce^{3+} concentration, the integrated total peak area is assumed to be proportional to [Ce^{3+}]. Two observations are worth mentioning.

First, the signal related to Ce^{3+} decreases with increasing O_2 exposure [inset (a) in Figure 2]. The decay at 300 K mirrors the increase of the superoxo signal [inset (a) in Figure 1]; this is not the case at higher temperatures, as seen below.

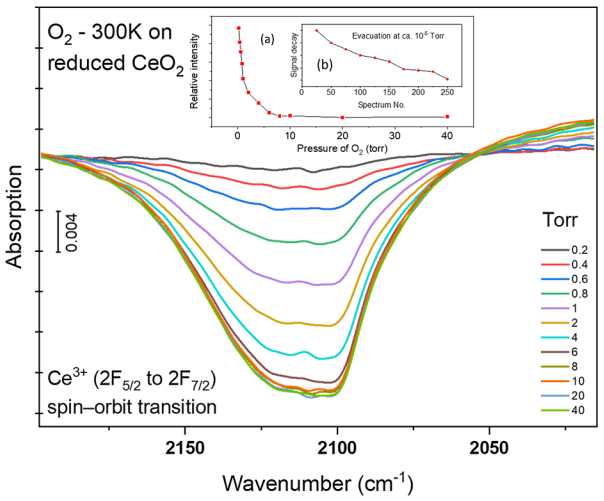

Figure 2. Changes of the Ce^{3+} ($^2F_{5/2}$ to $^2F_{7/2}$) spin−orbit electronic transition upon O_2 adsorption on reduced CeO_2 at 300 K at the indicated pressures. Near full oxidation is reached at ca. 10 Torr [inset (a)]. The inset (b) shows continued disappearance of the signal of the traces left of the signal upon evacuation at 300 K.

Second, the signal does not recover when the O_2 is pumped away; it continues to decrease [inset (b) in Figure 2]. This second observation indicates that the oxidation of Ce^{3+} cations is irreversible under the conditions of our experiment.

It is important to mention that, strictly, the surface is not oxidized due to the adsorption of O_2; this is because the overall charge would still be neutral

$$Ce^{3+} + O_2(g) \rightarrow Ce^{4+} + O_2^{\cdot-} \quad (1)$$

(charger per site = + 3)(charge per site = + 3)

It is only upon the reaction that oxidation takes place. In other words, the disappearance of the Ce^{3+} cations as tracked by IR in this work upon the exposure to O_2 is linked to the reaction-dynamic {the multiple steps involving adsorption, dissociation, and diffusion among other steps; the overall exothermic reaction of the oxidation of cerium sesquioxide [Ce(III) oxide] to cerium dioxide is $Ce_2O_3 + 1/O_2 \rightarrow 2\ CeO_2$, ΔH_r 298 K = −388.3 kJ/mol}.[41]

Next, the effect of exposing reduced CeO_2 to O_2 was studied at different temperatures, ranging from 300 to 423 K. Figure 3A shows the superoxo coverage profiles for three representative runs at 323, 373, and 398 K. As expected, it takes higher pressures (Figure S1) to reach surface saturation at higher temperatures (note the coverage profile shift to the right in Figure 3A). The isosteric heat of adsorption at different coverages is thus obtained from the plot of $[\mathrm{Ln}(P_{O_2})]_\theta$ as a function of $[1/T]_\theta$. It is found to be highly sensitive to the coverage. The extracted energy increases with increasing coverage. The inset in Figure 3A gives the obtained values at a high coverage. The scattering of the data at low coverage did not allow extraction of the adsorption energy. The energies ranged from 0.7 eV at near saturation to 0.4 eV at θ = 0.8.

Figure 3B presents the corresponding decay of the Ce^{3+} transition during the same experiment. While the profile mirrors that of the superoxo species at 323 K (similar to that found at 300 K), it deviates at higher temperatures. The disappearance of the Ce^{3+} signal has accelerated at high

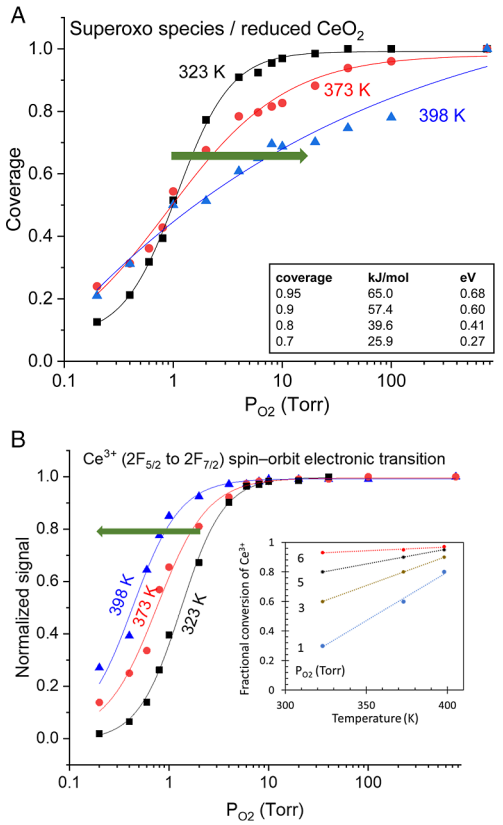

Figure 3. (A) Changes in surface coverage of the superoxo species as a function of P_{O_2} at the indicated temperatures. The inset shows the computed isosteric heat of adsorption obtained from a plot of $\mathrm{Ln}(P_{O_2})$ as a function of $1/T$. The green arrow points toward the need for higher pressures to saturate the surface. (B) Changes in the fraction of reacted Ce^{3+} ($^2F_{5/2}$ to $^2F_{7/2}$) spin–orbit electronic transition as monitored by DRIFT with P_{O_2} at the indicated temperatures. The inset shows the reacted fraction of Ce^{3+} as a function of temperature at the indicated pressures. The green arrow points to the opposite direction of that in (A) because of faster oxidation with increasing temperature.

temperatures; note the shift to the left side of the plots in Figure 3B. This fits with the dynamics of the reaction in which adsorbed oxygen molecules on the reduced CeO_2 will need to be dissociated and then diffuse to further oxidize subsurface Ce^{3+}. The diffusion energy barrier is higher than that of the dissociation–reduction of O_2[42] and therefore is poised to be more rate limiting. This is further highlighted in the inset in which the conversion of Ce^{3+} is plotted as a function of the temperature at different pressures. The slope decreases considerably with pressure. Data indicate that both the temperature and pressure have a cooperative effect on the oxidation of Ce^{3+}. At high temperatures, low pressures of O_2 are required for the oxidation process, while higher pressures are needed at low temperatures.

$$\frac{\Delta Ce^{3+}}{T} \propto P_{O_2} \qquad (2)$$

where ΔCe^{3+} is the difference between Ce^{3+} before ($[Ce^{3+}]P_{O_2=0}$) and after O_2 adsorption ($[Ce^{3+}]P_{O_2}$) at a given conversion as measured by the IR signal centered at ca. 2100 cm^{-1} attributed to ($^2F_{5/2}$ to $^2F_{7/2}$) spin–orbit electronic transition, T is the temperature, and P_{O_2} is the pressure of O_2 between 0.2 and 760 Torr.

This observation points out that the oxidation of Ce^{3+}, formed in the bulk of the powder particles by thermal reduction, is sensitive to oxygen diffusion from the surface to the bulk[43] (in the presence of molecular oxygen in the gas phase) to oxidize Ce^{3+} in the bulk, at the investigated temperatures.

The above results indicate that the observation of surface, near surface, or bulk oxygen defects (and/or associated Ce^{3+} cations) does not guarantee a specific catalytic (or photo/electro catalytic) activity because it is very sensitive to the reaction environment. Said differently, an initially highly defective binary oxide (such as in this case CeO_{2-x}) would become irreversibly oxidized very fast during the reaction in the presence of low partial pressure of molecular O_2, and therefore, associated catalytic cycles will stop in the absence of additional energy input (to regenerate the reduced states).

CONCLUSIONS

The adsorption of O_2 on reduced CeO_2 powders of about 10 nm in size, leading to the superoxo species, is studied at ambient pressures by DRIFTS at different temperatures and pressures. The reduced surface contained a pronounced IR signal in the 2050–2150 cm^{-1} region due to the ($^2F_{5/2}$ to $^2F_{7/2}$) spin–orbit electronic transition. The appearance of the 1125 cm^{-1} band of the superoxo is concomitant with the signal decay of the ($^2F_{5/2}$ to $^2F_{7/2}$) transition. The isosteric heat of adsorption of the peroxo adsorbate species, extracted from the $\mathrm{Ln}(P_{O_2})$ versus $1/T$, was equal to about 0.7 eV at near surface saturation. The profile of the decay of the electronic transition while sensitive to P_{O_2} changed with increasing temperatures. This indicates that the oxidation process is a function of atomic oxygen diffusion, in addition to the partial pressure of O_2 in the gas phase.

AUTHOR INFORMATION

Corresponding Authors

Hicham Idriss – *Institute of Functional Interfaces (IFG), Karlsruhe Institute of Technology (KIT), Eggenstein-Leopoldshafen 76344, Germany;* orcid.org/0000-0001-8614-7019; Email: Hicham.idriss@kit.edu

Christof Wöll – *Institute of Functional Interfaces (IFG), Karlsruhe Institute of Technology (KIT), Eggenstein-Leopoldshafen 76344, Germany;* orcid.org/0000-0003-1078-3304; Email: christof.woell@kit.edu

Authors

Lachlan Caulfield − *Institute of Functional Interfaces (IFG), Karlsruhe Institute of Technology (KIT), Eggenstein-Leopoldshafen 76344, Germany*

Eric Sauter − *Institute of Functional Interfaces (IFG), Karlsruhe Institute of Technology (KIT), Eggenstein-Leopoldshafen 76344, Germany*

Notes

The authors declare no competing financial interest.

ACKNOWLEDGMENTS

The authors thank Dr. Peter Weidler (IFG, KIT) for the XRD data and Dr. Mathias Schwotzer (IFG, KIT) for acquiring the SEM images of CeO_2.

REFERENCES

(1) Trovarelli, A. Catalytic Properties of Ceria and CeO_2-Containing Materials. *Catal. Rev.* **1996**, *38*, 439−520.

(2) Montini, T.; Melchionna, M.; Monai, M.; Fornasiero, P. Fundamentals and Catalytic Applications of CeO_2-Based Materials. *Chem. Rev.* **2016**, *116* (10), 5987−6041.

(3) Chueh, W. C.; Falter, C.; Abbott, M.; Scipio, D.; Furler, P.; Haile, S. M.; Steinfeld, A. High-Flux Solar-Driven Thermochemical Dissociation of CO_2 and H_2O Using Nonstoichiometric Ceria. *Science* **2010**, *330*, 1797−1801.

(4) Brugnoli, L.; Ferrari, A. M.; Civalleri, B.; Pedone, A.; Menziani, M. C. Assessment of Density Functional Approximations for Highly Correlated Oxides: The Case of CeO_2 and Ce_2O_3. *J. Chem. Theory Comput.* **2018**, *14*, 4914−4927.

(5) Li, P.; Chen, X.; Li, Y.; Schwank, J. W. A review on oxygen storage capacity of CeO_2-based materials: Influence factors, measurement techniques, and applications in reactions related to catalytic. *Catal. Today* **2019**, *327*, 90−115.

(6) Paparazzo, E. Use and mis-use of x-ray photoemission spectroscopy Ce3d spectra of Ce_2O_3 and CeO_2. *J. Phys.: Condens. Matter* **2018**, *30*, 343003.

(7) Rakhmatullin, R.; Semashko, V.; Korableva, S.; Kiiamov, A.; Rodionov, A.; Tschaggelar, R.; van Bokhoven, J.; Paun, C. EPR study of ceria nanoparticles containing different concentration of Ce^{3+} ions. *Mater. Chem. Phys.* **2018**, *219*, 251−257.

(8) Yuán, S.; Xu, B.; Zhang, Q.; Liu, S.; Xie, J.; Zhang, M.; Ohno, T. Development of the Visible-Light Response of CeO_{2-x} with a high Ce^{3+} Content and Its Photocatalytic Properties. *ChemCatChem* **2018**, *10*, 1267−1271.

(9) Tamura, M.; Tomishige, K. Redox Properties of CeO_2 at Low Temperature: The Direct Synthesis of Imines from Alcohol and Amine. *Angew. Chem., Int. Ed.* **2015**, *54*, 864−827.

(10) Zhang, M.; Zhang, S.; Qi, Z.; Xie, M.; Qu, Y. Recent advancements of CeO_2-enabled liquid acid/base catalysis. *Catal. Sci. Technol.* **2024**, *14*, 225−240.

(11) Wang, Z.-Q.; Chu, D.-R.; Zhou, H.; Wu, X.-P.; Gong, X.-Q. Role of Low-Coordinated Ce in Hydride Formation and Selective Hydrogenation Reactions on CeO_2 Surfaces. *ACS Catal.* **2022**, *12*, 624−632.

(12) Zhou, C.-Y.; Wang, D.; Gong, X.-Q. A DFT+ U revisit of reconstructed CeO_2 (100) surfaces: Structures, thermostabilities and reactivities. *Phys. Chem. Chem. Phys.* **2019**, *21*, 19987−19994.

(13) Zhang, K.; Li, G.; Zou, C.; Chen, S.; Li, S.; Han, Z.-K.; Jiang, Y.; Yuan, W.; Yang, H.; Ganduglia-Pirovano, M. V.; Wang, Y. A CeO_2 (100) surface reconstruction unveiled by in situ STEM and particle swarm optimization techniques. *Sci. Adv.* **2024**, *10*, 1−7.

(14) Idriss, H. Oxygen vacancies role in thermally driven and photon driven catalytic reactions. *Chem Catal.* **2022**, *2*, 1549−1560.

(15) *The LibreTexts libraries are Powered by NICE CXone Expert and are supported by the Department of Education Open Textbook Pilot Project, the UC Davis Office of the Provost, the UC Davis Library*; The California State University: USA, 2023.

(16) Han, Z.-K.; Zhang, L.; Liu, M.; Ganduglia-Pirovano, M. V.; Gao, Y. The Structure of Oxygen Vacancies in the Near-Surface of Reduced CeO_2 (111) Under Strain. *Front. Chem.* **2019**, *7*, 436.

(17) Scaranto, J.; Idriss, H. *Top. Catal.* **2015**, *58*, 143−148.

(18) Ganduglia-Pirovano, M. V.; Murgida, G. E.; Ferrari, V.; Llois, A. M. Comment on "Oxygen Vacancy Ordering and Electron Localization in CeO_2: Hybrid Functional Study. *J. Phys. Chem. C* **2017**, *121* (38), 21080−21083.

(19) Ganduglia-Pirovano, M. V.; Da Silva, J. L. F.; Sauer, J. Density-Functional Calculations of the Structure of Near-Surface Oxygen Vacancies and Electron Localization on CeO_2(111). *Phys. Rev. Lett.* **2009**, *102*, 026101.

(20) Andersson, D. A.; Simak, S. I.; Skorodumova, N. V.; Abrikosov, I. A.; Johansson, B. Redox properties of CeO_2−MO_2 (M= Ti, Zr, Hf, or Th) solid solutions from first principles calculations. *Appl. Phys. Lett.* **2007**, *90*, 031909.

(21) Descorme, C.; Madier, Y.; Duprez, D. Infrared Study of Oxygen Adsorption and Activation on Cerium−Zirconium Mixed Oxides. *J. Catal.* **2000**, *196*, 167−173.

(22) Li, C.; Domen, K.; Maruya, K.-i.; Onishi, T. Dioxygen adsorption on well-outgassed and partially reduced cerium oxide studied by FT-IR. *J. Am. Chem. Soc.* **1989**, *111*, 7683−7687.

(23) Li, C.; Domen, K.; Maruya, K.-i.; Onishi, T. IR spectra of dioxygen species formed on CeO_2 at room temperature. *J. Chem. Soc., Chem. Commun.* **1988**, 1541−1542.

(24) Soria, J.; Martinez-Arias, A.; Conesa, J. C. Spectroscopic study of oxygen adsorption as a method to study surface defects on CeO_2. *J. Chem. Soc. Faraday Trans.* **1995**, *91*, 1669−1678.

(25) Choi, Y. M.; Abernathy, H.; Chen, H.-T.; Lin, M. C.; Liu, M. Characterization of O_2−CeO_2 Interactions Using In Situ Raman Spectroscopy and First-Principle Calculations. *ChemPhysChem* **2006**, *7*, 1957−1963.

(26) Yang, C.; Yu, X.; Heißler, S.; Weidler, P. G.; Nefedov, A.; Wang, Y.; Wöll, C.; Kropp, T.; Paier, J.; Sauer, J. O_2 Activation on Ceria Catalysts—The Importance of Substrate Crystallographic Orientation. *Angew. Chem., Int. Ed.* **2017**, *56*, 16399−16404.

(27) Preda, G.; Migani, A.; Neyman, K. M.; Bromley, S. T.; Illas, F.; Pacchioni, G. Formation of Superoxide Anions on Ceria Nanoparticles by Interaction of Molecular Oxygen with Ce^{3+} Sites. *J. Phys. Chem. C* **2011**, *115*, 5817−5822.

(28) Wu, W.; Savereide, L. M.; Notestein, J.; Weitz, E. In-situ IR spectroscopy as a probe of oxidation/reduction of Ce in nanostructured CeO_2. *Appl. Surf. Sci.* **2018**, *445*, 548−554.

(29) Afrin, S.; Bollini, P. On the Utility of Ce^{3+} Spin−Orbit Transitions in the Interpretation of Rate Data in Ceria Catalysis: Theory, Validation, and Application. *J. Phys. Chem. C* **2023**, *127*, 234−247.

(30) Salusso, D.; Mauri, S.; Deplano, G.; Torelli, P.; Bordiga, S.; Rojas-Buzo, S. MOF-Derived CeO_2 and CeZrOx Solid Solutions: Exploring Ce Reduction through FTIR and NEXAFS Spectroscopy. *Nanomaterials* **2023**, *13*, 272.

(31) Chakarova, K.; Drenchev, N.; Mihaylov, M.; Hadjiivanov, K. Interaction of O_2 with Reduced Ceria Nanoparticles at 100−400 K: Fast Oxidation of Ce^{3+} Ions and Dissolved H_2. *Catalysts* **2024**, *14*, 45.

(32) Vissers, G. O.; Zhang, W.; Vilches, O. E.; Liu, W.-G.; Yu, H. S.; Truhlar, D. G.; Campbell, C. T. Heats of Adsorption of N_2, CO, Ar, and CH_4 versus Coverage on the Zr-Based MOF NU-1000: Measurements and DFT Calculations. *J. Phys. Chem. C* **2019**, *123*, 6586−6591.

(33) Dhouib, A.; Mezghrani, B.; Finocchiaro, G.; Le Borgne, R.; Berthet, M.; Daydé-Cazals, B.; Graillot, A.; Ju, X.; Berret, J.-F. Synthesis of Stable Cerium Oxide Nanoparticles Coated with Phosphonic Acid-Based Functional Polymers. *Langmuir* **2023**, *39*, 8141−8152.

(34) Molinet-Chinaglia, C.; Cardenas, L.; Vernoux, P.; Piccolo, L.; Loridant, S. Tuning the metal loading of Pt/CeO_2 catalysts for the water-gas shift reaction. *Mater. Today Catal.* **2024**, *4* (1−11), 100046.
(35) Chen, H.-L.; Chen, H.-T. Role of hydroxyl groups for the O_2 adsorption on CeO_2 surface: A DFT + U study. *Chem. Phys. Lett.* **2010**, *493*, 269−272.
(36) Nuhnen, A.; Janiak, C. A practical guide to calculate the isosteric heat/enthalpy of adsorption via adsorption isotherms in metal−organic frameworks, MOFs. *Dalton Trans.* **2020**, *49*, 10295−10307.
(37) Turner, S.; Lazar, S.; Freitag, B.; Egoavil, R.; Verbeeck, J.; Put, S.; Strauven, Y.; Van Tendeloo, G. High resolution mapping of surface reduction in ceria nanoparticles. *Nanoscale* **2011**, *3*, 3385−3390.
(38) Yang, C.-W.; Yu, X.; Heißler, S.; Nefedov, A.; Colussi, S.; Llorca, J.; Trovarelli, A.; Wang, Y.; Wöll, C. Surface faceting and reconstruction of ceria nanoparticles. *Angew. Chem., Int. Ed.* **2017**, *56*, 375−379.
(39) Zhang, Y. C.; Lei, M.; Huang, K.; Liang, C.; Wang, Y. J.; Ding, S. S.; Zhang, R.; Fan, D. Y.; Yang, H. J.; Wang, Y. G. A facile route to mono-dispersed CeO_2 nanocubes and their enhanced photocatalytic properties. *Mater. Lett.* **2014**, *116*, 46.
(40) Crozier, A.; Wang, R.; Sharma, R. In situ environmental TEM studies of dynamic changes in cerium-based oxides nanoparticles during redox processes. *Ultramicroscopy* **2008**, *108*, 1432−1440.
(41) Huntelaar, M. E.; Booij, A. S.; Cordfunke, E. H. P.; van der Laan, R. R.; van Genderen, A. C. G.; van Miltenburg, J. C. The thermodynamic properties of Ce_2O_3 (s) from$T\rightarrow$ 0 to 1500 K. *J. Chem. Thermodyn.* **2000**, *32*, 465−482.
(42) Chen, H.-T.; Chang, J.-G.; Chen, H.-L.; Ju, S.-P. Identifying the O_2 diffusion and reduction mechanisms on CeO_2 electrolyte in solid oxide fuel cells: A DFT + U study. *J. Comput. Chem.* **2009**, *30*, 2433−2442.
(43) Perkins, C. L.; Henderson, M. A.; Peden, C. H. F.; Herman, G. S. Self-diffusion in ceria. *J. Vac. Sci. Technol., A* **2001**, *19*, 1942−1946.